


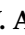



Article

Benzylidene Cyclopentanone Derivative Photoinitiator for Two-Photon Photopolymerization-Photochemistry and 3D Structures Fabrication for X-ray Application

Anton E. Egorov ^{1,*} , Alexey A. Kostyukov ¹ , Denis A. Shcherbakov ² , Danila A. Kolymagin ²,
Dmytro A. Chubich ², Rilond P. Matital ² , Maxim V. Arsenyev ³ , Ivan D. Burtsev ¹, Mikhail G. Mestergazi ^{1,4},
Elnara R. Zhiganshina ³, Sergey A. Chesnokov ³, Alexei G. Vitukhnovsky ^{1,5,*} and Vladimir A. Kuzmin ¹

¹ N. M. Emanuel Institute of Biochemical Physics, Russian Academy of Sciences, 119334 Moscow, Russia

² Moscow Institute of Physics and Technology, National Research University, Institutskii per. 9, 141700 Dolgoprudny, Russia

³ G. A. Razuvaev Institute of Organometallic Chemistry, Russian Academy of Sciences, 603950 Nizhny Novgorod, Russia

⁴ Department of Medicinal Chemistry, Ernest Mario School of Pharmacy, Rutgers, The State University of New Jersey, Piscataway, NJ 08854, USA

⁵ Lebedev Physical Institute, Russian Academy of Sciences, Leninskii Prospect 53, 119991 Moscow, Russia

* Correspondence: ae.yegorov@gmail.com (A.E.E.); vitukhnovsky@mail.ru (A.G.V.)

Abstract: Micron- and submicron-scale 3D structure realization nowadays is possible due to the two-photon photopolymerization (TPP) direct laser writing photolithography (DLW photolithography) method. However, the achievement of lithographic features with dimensions less than 100 nm is in demand for the fabrication of micro-optical elements with high curvature values, including X-ray microlenses. Spectroscopic and photochemical study of a photoinitiator (PI) based on a methyl methacrylate derivative of 2,5-bis(4-(dimethylamino)benzylidene) cyclopentanone was performed. Enhanced intersystem crossing in the methyl methacrylate derivative results in increased radical generation for the subsequent initiation of polymerization. A comprehensive study of the new photocompositions was performed, with particular emphasis on photochemical constants, the degree of photopolymerization, and topology. The optimal parameters for the fabrication of mechanically stable structures were determined in this research. The threshold dose parameters for lithography (radiation power of 5 mW at a speed of 180 $\mu\text{m/s}$) when trying to reach saturation values with a conversion degree of $(35 \pm 1)\%$ were defined, as well as parameters for sub-100 nm feature fabrication. Moreover, the 45 nm feature size for elements was reached. Fabrication of X-ray lens microstructures was also demonstrated.

Keywords: benzylidene ketone; photoinitiator; triplet state; two-photon photopolymerization (TTP); direct laser writing photolithography (DLW photolithography); X-ray microlenses



Citation: Egorov, A.E.; Kostyukov, A.A.; Shcherbakov, D.A.; Kolymagin, D.A.; Chubich, D.A.; Matital, R.P.; Arsenyev, M.V.; Burtsev, I.D.; Mestergazi, M.G.; Zhiganshina, E.R.; et al. Benzylidene Cyclopentanone Derivative Photoinitiator for Two-Photon Photopolymerization-Photochemistry and 3D Structures Fabrication for X-ray Application. *Polymers* **2023**, *15*, 71. <https://doi.org/10.3390/polym15010071>

Academic Editor: Jacques Lalevee

Received: 9 December 2022

Revised: 21 December 2022

Accepted: 22 December 2022

Published: 24 December 2022



Copyright: © 2022 by the authors. Licensee MDPI, Basel, Switzerland. This article is an open access article distributed under the terms and conditions of the Creative Commons Attribution (CC BY) license (<https://creativecommons.org/licenses/by/4.0/>).

1. Introduction

Two-photon photopolymerization (TPP, DLW photolithography) is a unique technology that allows for the fabrication of polymeric 3D structures with the required submicron spatial resolution in terms of their morphology and topology. This technology is based on two-photon absorption of a focused femtosecond laser radiation by a photosensitive component (photoinitiator), which initiates the polymerization reaction. As a result, a polymerized element is formed in the focal region. Because two-photon absorption probability is proportional to the squared intensity of light, the excitation volume is confined mostly to the focal spot. Due to this peculiarity, TPP makes it possible to diminish voxel (a 3D analogue of a pixel in photography) size, an advantage compared to one-photon polymerization processes. Moreover, the use of NIR femtosecond laser excitation sources allows for increased penetration depth since most of the polymers are near transparent in this spectral

region [1,2]. Due to the possibility of achieving submicron elements for 3D structures, DLW photolithography and two-photon absorption techniques have found application in such areas as the development of photonic crystals [3,4], microrobotics and metamaterials [5–7], biomedicine [8], microfluidics research [9,10], micro-optics [11–15], hydrogel nanoarchitecture [16], and photovoltaics [17]. Recently, the possibility of fabricating X-ray microlenses using DLW photolithography was demonstrated. Such structures allow for X-ray radiation to be focused at a distance of 120 mm (numerical aperture $NA = 1.7 \times 10^{-4}$) into a spot with a diameter of less than 500 nm [18]. The advantage of such an approach is that a microlens system with an arbitrary curvature radius can be fabricated using DLW photolithography. It is possible to improve the quality of such structures through investigation of the material's properties after the pyrolysis process [19]. However, further research is required to reduce voxel size in order to achieve an increase in the numerical aperture of these objects.

Photoinitiators based on benzylidene ketone moiety are promising for photocomposition preparation [20]. Single-component photoinitiation systems greatly simplify preparation. The bis-benzylidene ketone carcass is an example of a D- π -A- π -D system where electron donors and accepting groups are bridged with a π -conjugated chain. By changing the length of the π -conjugated chain of the dye, one can shift the absorption band, thus varying the depth of light penetration and enabling visible light polymerization. This capability, along with intensive molar extinction (up to $1 \times 10^5 \text{ M}^{-1} \text{ cm}^{-1}$), makes these dyes versatile in the photoinitiation process. The molecule possesses both electron-withdrawing (carbonyl) and electron donor (amino) groups, resulting in a charge transfer process. Bis-benzylidene ketone dyes possess the ability to initiate both one- and two-photon polymerization processes [20]. These PIs undergo photobleaching during the photopolymerization process [21]. This feature could be beneficial because no decrease in photopolymerization process speed due to absorption of the dye takes place. The facile synthesis process of these compounds is another trait that makes these PIs attractive.

In this paper, the photochemistry of bis-(dimethylaminoarylidene) cyclopentanone containing four methyl methacrylate groups (4Met-BAC) was compared to the widely known molecule 2,5-bis(4-(dimethylamino)benzylidene) cyclopentanone (MBAC) and was investigated (Figure 1). The two-photon polymerization process was demonstrated using a 4Met-BAC PI. The introduction of methyl methacrylate groups into the PI molecule allows for increased solubility of the PI in monomer due to the chemical similarity that is gained. A comprehensive study of PI photochemistry and the mechanical and morphological properties of 3D nanosized structures made it possible to determine the optimal characteristics of new photocompositions.

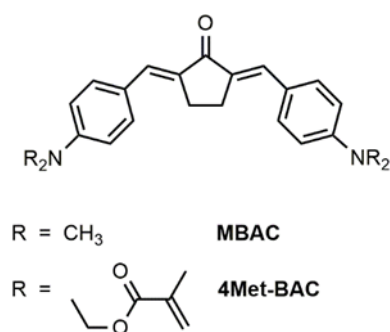


Figure 1. Molecular structure of MBAC and 4Met-BAC photoinitiators.

2. Materials and Methods

2.1. Materials

Solvents for spectroscopic studies were spectroscopic grade (Komponent-Reaktiv, Moscow, Russia), and others were purified by the standard methods [22]. The monomer pentaerythritol triacrylate (PETA) (“Aldrich”) was used without additional purification. MBAC was

synthesized by the well-known procedure [23]. (4-Formylphenyl)azandiylbis(ethane-2,1-diyl)dibenzoate was prepared according to the procedure described in [24].

2.2. Synthesis of 4Met-BAC

(((1E,1'E)-(2-oxocyclopentane-1,3-diylidene)bis(methanylylidene))bis(4,1-phenylene))bis(azanetriyl)tetrakis(ethane-2,1-diyl) tetra-kis(2-methylacrylate) (4Met-BAC). To a suspension of benzylidenecyclopentanone tetraol (2.33 g, 5 mmol) and K_2CO_3 (10.4 g, 7.5 mmol) in dichloromethane (100 mL), a solution of methacryloyl chloride (2.05 mL, 21 mmol) in dichloromethane (20 mL) was added dropwise with cooling. The mixture was stirred for 24 h and the precipitate was filtered. Hexane (30 mL) was added to the filtrate and the product was crystallized, filtered, and dried in vacuo. Orange-red fine crystalline powder with a yield of 2.66 g (72%) was obtained. Elements found: C, 69.95; H, 6.89; N, 3.71. Calc. for $C_{43}H_{50}N_2O_9$: C, 69.90; H, 6.82; N, 3.79 %. 1H -NMR (300 MHz, $CDCl_3$), δ (ppm): 1.93 (s, 12H, CH_3 (meth)), 3.06 (s, 4H, CH_2 (c-pentanone)), 3.75 (t, 8H, OCH_2 , $J = 6.2$ Hz), 4.35 (t, 8H, NCH_2 , $J = 6.2$ Hz), 5.59 (s, 4H, $C_{Met}H$), 6.09 (s, 4H, $C_{Met}H$), 6.84 (d, 4H, C_{Ar} , $J = 8.9$ Hz), 7.52 (s, 2H, $OCC=CH$), 7.54 (d, 4H, C_{Ar} , $J = 8.9$ Hz). ^{13}C -NMR (75 MHz, $CDCl_3$), δ (ppm): 196.11, 167.30, 148.00, 135.89, 134.01, 133.26, 132.82, 126.20, 125.12, 111.97, 61.54, 49.43, 26.62, 18.36. IR (Nujol, ν/cm^{-1}): 1375, 1457, 1522, 1590, 1678, 1715, 2927, 3400 (Figures S1 and S2).

2.3. Absorption Spectroscopy

UV-vis absorption spectra were recorded on a Shimadzu UV-3101 PC spectrophotometer in the range from 350 to 700 nm in quartz cells with an optical pathlength of 1 cm, unless otherwise noted.

2.4. Fluorescence Spectroscopy

Fluorescence measurements and singlet oxygen luminescence experiments were performed with a FluoTime 300 fluorescence lifetime spectrometer (PicoQuant GmbH, Berlin, Germany). For fluorescence quantum yield determination experiments, compound solutions of matched optical density (<0.05 per cm) were used at an excitation wavelength of 491 nm. Fluorescence lifetime measurements were made through picosecond time-correlated single-photon counting (TCSPC) and a pulsed laser light source (475 nm). Emission data were collected at 600 nm. The instrument response function (IRF) was recorded with the use of a Ludox probe. For singlet oxygen luminescence detection experiments, a spectrometer equipped with the NIR PMT Module H10330-45 (Hamamatsu, Japan) coupled to the single-photon counter TimeHarp TCSPC (PicoQuant GmbH, Berlin, Germany) was used. Singlet oxygen luminescence experiments were performed using a quartz cuvette with a 1 cm optical path. The excitation source used was a Xe lamp (438–470 nm).

2.5. Flash Photolysis

The transient absorption spectra of radical intermediates were measured using a conventional flash photolysis setup (LLC "MELZ", Moscow, Russia) (optical path length 20 cm, excitation performed through multi-band blue-green optical absorption filters 420–550 nm, 80 J/15 μ s). Signals were recorded using a PMT-38 photomultiplier (LLC "MELZ", Moscow, Russia) at 400–600 nm.

2.6. Laser Flash Photolysis

Laser pulse photolysis was carried out on an LKS 80 (Applied Photophysics, Leatherhead, UK) laser pulse photolysis setup. The third harmonics of a Nd-YAG laser (Brilliant B, Quantel, LUMIBIRD, Cournon-d'Auvergne, France) was used for excitation. Excitation wavelength in the range 420–600 nm was tuned by an OPO (MagicPrism, OPOTEK Inc., Carlsbad, CA, USA). Kinetics of transient species generated by a 5 ns laser excitation pulse were registered by difference absorbance changes in the spectral range of 400–750 nm using a 150 Xe arc lamp with 50-fold beam overdrive and 1.5 ms capacitor discharge. The detection system was equipped with a 600 MHz oscilloscope (Agilent Infiniium 10 GS/s) and

an R928-type PMT. The kinetic data were processed through global analysis by fitting the kinetic traces over the whole range of the registration wavelengths with a multiexponential equation (Equation (1)):

$$\Delta A_{\lambda} = \sum \Delta A_{\lambda_i} \exp(-t/\tau_i) \quad (1)$$

where ΔA_{λ} is the overall difference absorbance at the registration wavelength λ , ΔA_{λ_i} is the absorbance of the i -th transient species at the registration wavelength λ , and $\tau_i = 1/k_i$ is the lifetime of the i -th transient species, with τ_i and ΔA_{λ_i} being the fitting parameters. The accuracy in the lifetime determination was 15%.

2.7. DLW Photolithography

In this research, polymer structures were fabricated using DLW photolithography. The fabrication was carried out with a commercial setup (Nanoscribe Professional GmbH, Nanoscribe, Eggenstein-Leopoldshafen, Germany). The initiating two-photon photopolymerization reaction involved femtosecond laser radiation with an 80 MHz repetition rate and a 780 nm wavelength λ . This radiation was focused with a Zeiss high-aperture planapochromatic objective (NA = 1.4, 63). A new photosensitive composition based on the photoinitiator 4Met-BAC with methyl groups (1% wt) was used as a negative photoresin. Samples were developed in propylene glycol monomethyl ether acetate (PEGMA) for 25 min and then in isopropyl alcohol (IPA) for 5 min after the DLW lithography process.

2.8. Morphology

The influence of DLW photolithography parameters on the obtained voxel lithography element's physical properties was investigated. The atomic force microscopy method (AFM, Solver Pro M, NT-MDT) was employed to study the axial size of a voxel. Measurements were carried out in a semicontact scanning mode. Scanning electron microscopy (SEM JEOL JSM-7001F, MIPT CUC, JEOL Ltd., Tokyo, Japan) was used to characterize the smallest axial size of the polymerized elements. A sample was prepared for morphological study. This sample contained arrays of linear voxel elements which were made with different output laser radiation powers. Within the array, the lithography linear velocity was varied to change the exposure time.

2.9. Confocal Laser Scanning Microscopy (CLSM)

Commercial Confocal Laser Scanning Microscopy (CLSM510, Carl Zeiss, Jena, Germany) was employed for the examination of the fabricated 3D polymer X-ray microlenses. Measurement of the 3D image along the z -axis was carried out using a scan mode Z-stack, with an excitation laser at 458 nm and a 40 \times /1.3 (Plan-Neofluar 40 \times /1.3, Carl Zeiss, Jena, Germany) oil immersion objective lens. Detection of the luminescence signal of the 3D polymer structure was carried out at the wavelength of 488 nm using a spectral long pass filter with a transmission wavelength of 505 nm and photomultiplier tubes which were equipped in the microscope.

2.10. Raman Spectroscopy

The spectroscopic properties of the polymerized and non-polymerized photocomposition were investigated using Raman spectroscopy. The measurements were carried out using a Horiba JY LabRAM HR Evolution Raman spectroscopy setup (Horiba, Kyoto, Japan). The laser wavelength was 633 nm, average laser power was 3.5 mW, and the grating was 1800 grooves/mm. One Raman spectrum was recorded with an exposure time of 70 s and averaged over 2 acquisitions.

3. Results

3.1. Spectroscopic Studies

3.1.1. Absorption and Fluorescence Spectroscopy

Having an electron-donating amino group and electron-accepting carbonyl group results in charge transfer in photoinitiator molecules. Due to intramolecular charge transfer of

the excited-state dyes, substantial positive solvatochromism could be observed (Figure 2a,b, Table 1). With the increase in solvent polarity, bathochromic shift of both absorption and emission spectra took place, confirming that S_1 is of (π, π^*) type [25].

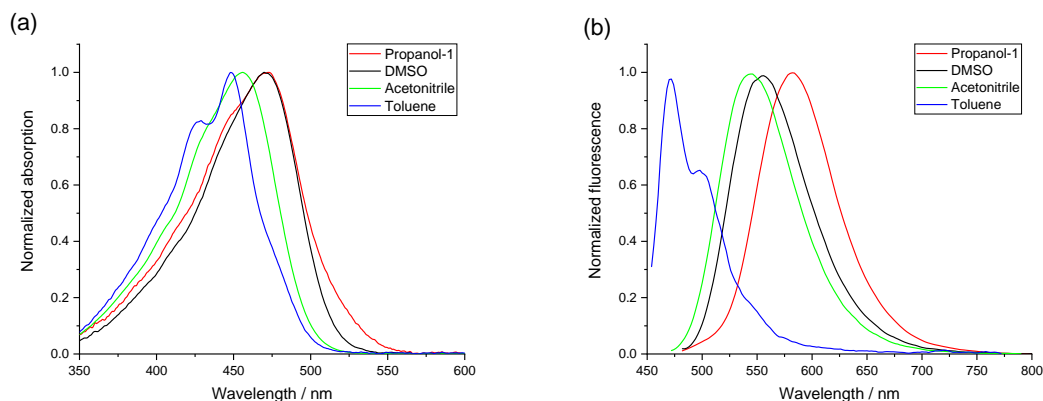


Figure 2. (a) Normalized 4Met-BAC absorption spectra in different solvents. (b) Normalized 4Met-BAC fluorescence spectra in different solvents.

Table 1. Absorption and emission data of 4Met-BAC in different solvents.

Solvent	$\lambda_{\text{abs}}/\text{nm}$	$\lambda_{\text{flu}}/\text{nm}$	$\Delta\nu/\text{cm}^{-1}$	F
Toluene	448	472	1135	0.029
DMSO	474	558	3176	0.841
Propanol-1	473	584	4063	0.779
Acetonitrile	459	544	3404	0.860
Dichloromethane	456	528	2990	0.592
Ethyl acetate	448	514	2866	0.489
Acetone	454	539	3473	0.790

In nonpolar aprotic solvents such as toluene, the fluorescence quantum yield decreases with the introduction of methacrylate groups into ketocyanine dye molecules (Table 2). The reason for this is the partial disruption of molecule planarity and the increase in vibrational relaxation processes. In protic polar solvent such as propanol-1, the excited-state dye is stabilized by both hydrogen bonding and dipole–dipole interaction. The red shift in both absorption and fluorescence spectra is the most pronounced in propanol-1, despite the relatively low dielectric constant compared to DMSO. This is due to lowering of the excited energy levels in solvent–solute complexes.

Table 2. Photochemical characteristics of studied compounds in different solvents.

Solvent	Compound	Φ_{Δ}	Φ_{flu}	$\tau_{\text{flu}}/\text{ns}$
Acetonitrile	MBAC	0.14	0.10	0.67
	4Met-BAC	0.17	0.11	0.71
Toluene	MBAC	0.16	0.08	0.30
	4Met-BAC	0.11	0.05	0.24
Propanol-1	MBAC	0.05	0.15	0.46
	4Met-BAC	0.08	0.35	1.16
DMSO	MBAC	-	0.17	0.78
	4Met-BAC	-	0.20	0.84

Electronic interactions between polar solvent molecules and polar solute play an important role in stabilization of the excited state. In the case of protic solvents, hydrogen bonding also takes place. These effects could be observed in fluorescence lifetime measurements (Table 2). The most short-lived MBAC and 4-Met-BAC fluorescence belongs to the toluene solution (in highly polar acetonitrile it is almost three times larger). An interesting observation is made for propanol-1 solution. While 4Met-BAC and MBAC fluorescence lifetime is slightly different among nonprotic solvents, in propanol-1 solution the distinction is more prominent (0.46 ns vs. 1.16 ns) (Figure 3a), which also affects the difference between fluorescence quantum yields as well.

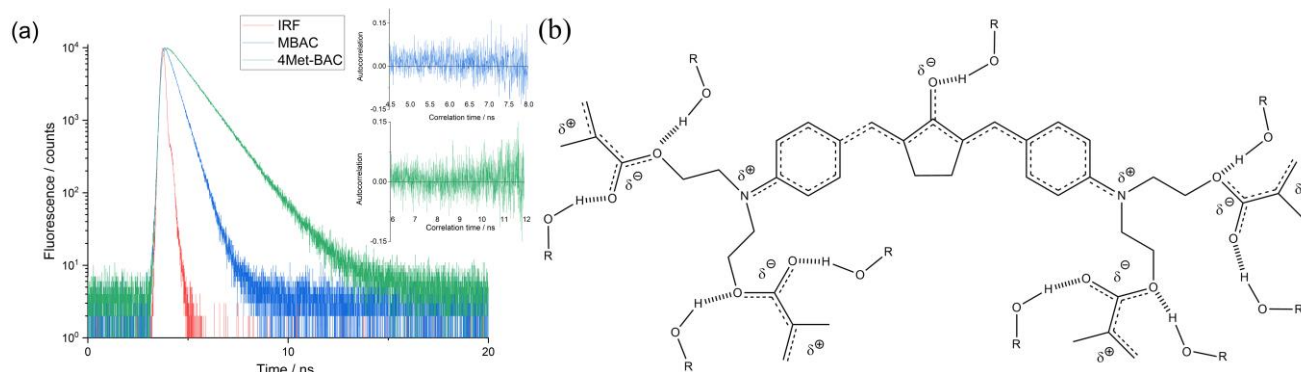


Figure 3. (a) Fluorescence kinetics decay of MBAC (blue) and 4Met-BAC (green) in propanol; excitation 475 nm. (b) Proposed hydrogen bonding of 4Met-BAC molecules in alcohol solvent.

Alcohol hydrogen bonding ability towards the ketocyanine dye carbonyl group was previously established [26]. 4Met-BAC bears not only the central carbonyl group, but also the four methacrylic ester groups. The latter are capable of hydrogen bonding with alcohol molecules (Figure 3b). Thus, the multiplication of a hydrogen bond number in the case of 4Met-BAC results in amplified fluorophore stabilization and increases in fluorescence lifetime.

Spectral shifts with the increase in solvent polarity are more pronounced for fluorescence than absorption. This indicates that the excited state dipole moment is larger than ground state one.

3.1.2. Excited State Dipole Moment

Intramolecular charge transfer results in reorientation of solvent molecules surrounding the solute [27]. The excited state dipole moment was calculated according to Bakhshiev's formula [28]:

$$v_a - v_f = \frac{2\Delta\mu^2}{a_0^3hc} F \quad (2)$$

where,

$$F = \left(\frac{D-1}{D+2} - \frac{n^2-1}{n^2+2} \right) \cdot \frac{(2n^2+1)}{(n^2+2)} \quad (3)$$

where $\Delta\mu^2 = (\mu_e - \mu_g)^2$, v_a and v_f are absorption and emission maxima wavenumbers, μ_e and μ_g are the excited and ground singlet state dipole moment, respectively, a_0 is the solute cavity radius, h is Planck's constant, c is the speed of light, and D and n are the relative permittivity and refractive index, respectively.

The plot of Stokes shift versus F (Figure 4) yields a slope from which μ_e can be calculated:

$$\text{Slope} = \frac{2(\mu_e - \mu_g)^2}{a_0^3hc} \quad (4)$$

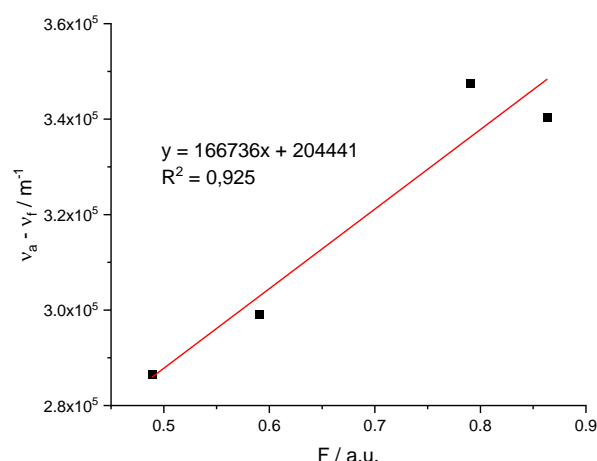


Figure 4. Plot between solvent spectral shifts and F solvent term for 4Met-BAC.

Protic and nonpolar solvents were excluded since a different kind of interaction takes place.

The solute cavity radius for 4Met-BAC was estimated according to [29] using the density of benzophenone. The ground state dipole moment was calculated using Hyperchem 8.0 software. Semiempirical calculations utilizing the INDO method to optimize molecular geometry resulted in 4.2 D and 4.5 D for 4Met-BAC and MBAC molecules, respectively, which is in accordance with [30,31]. The excited state dipole moment was estimated to be 10.8 D for 4Met-BAC, while for non-substituted MBAC it was estimated by another group to be 10.4 D [30]. The results show no substantial change in excited state dipole moment upon introduction of four methacrylic ester groups since the electron-donating ability of substituents is close.

3.1.3. HOMO-LUMO

Quantum chemical calculation of 4Met-BAC was performed using the ORCA 4.0.1.2 program package and density functional theory at the B3LYP functional with a 6-31G(d) basis set. 4Met-BAC's structure has a planar geometry excluding peripheral methyl methacrylate substituents (Figure 5).

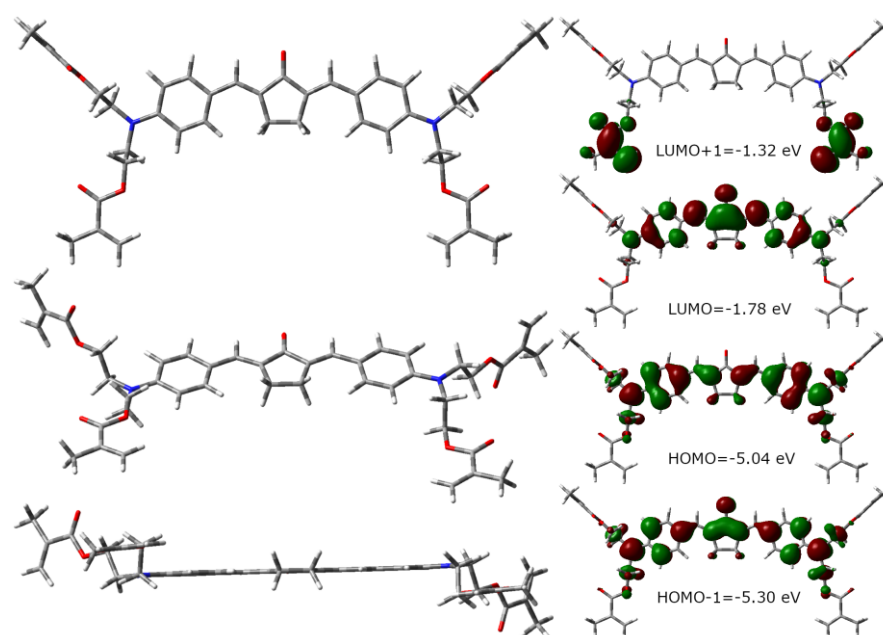


Figure 5. Optimized structure and molecular orbitals of 4Met-BAC.

The HOMO and HOMO-1 orbitals have π symmetry, with the electrons distributed through the whole conjugated π system. The HOMO π electron shows an interruption of the conjugation at the carbonyl group. LUMO level is mainly located at carbonyl and cyclopentanone groups. These electron density distributions indicate that HOMO \Rightarrow LUMO transitions comprise intermolecular charge transfer.

3.1.4. Triplet State Investigation

Laser flash photolysis experiments were conducted with 4Met-BAC in different solvents. In all cases, triplet–triplet absorption spectra include photobleaching of the singlet state, with position corresponding to the singlet absorption spectra. Longer wavelength regions demonstrate triplet absorption that gradually intensifies with the increasing wavelength (Figure 6a,b).

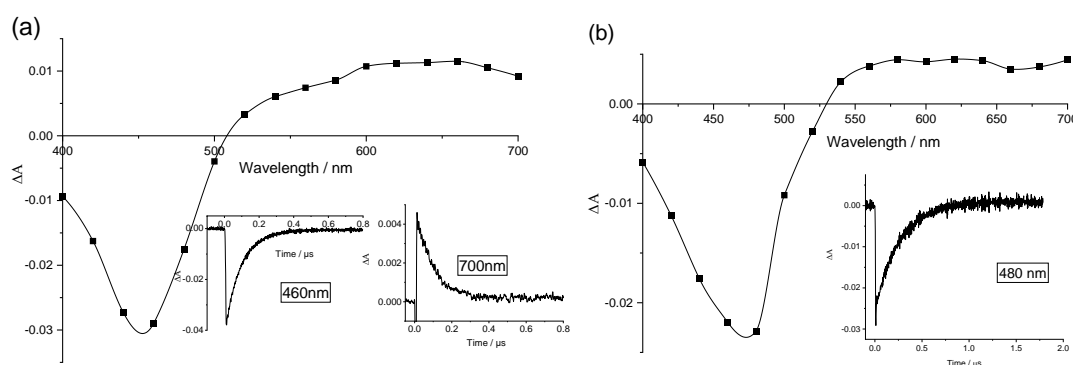


Figure 6. (a) Differential triplet–triplet absorption spectrum for 4Met-BAC (8.0×10^{-6} M) in acetonitrile (air-equilibrated) at 35 ns after flash. Excitation at 455 nm. Inserts show photobleaching of the singlet state at 460 nm and decay of the triplet state of 4Met-BAC at 700 nm ($k = 1.1 \times 10^7$ s $^{-1}$). (b) Differential triplet–triplet absorption spectrum for 4Met-BAC (8.0×10^{-6} M) in propanol-1 (air-equilibrated) at 50 ns after flash. Excitation at 475 nm. Insert shows 4Met-BAC singlet state photobleaching at 480 nm ($k = 3.8 \times 10^6$ s $^{-1}$).

In order to estimate triplet generation efficiency in every solvent, 4Met-BAC solutions with equal optical density at the excitation wavelength were prepared. Obtained triplet absorption maxima were compared in toluene, acetonitrile, and propanol-1. Triplet state generation ability is the most prominent in acetonitrile, closely followed by toluene; in the case of propanol-1 it is around 2.5 times less compared to acetonitrile. These results agree with the triplet state quantum yield determination experiments for MBAC derivatives [31]. The presence of carbonyl groups introduces excited (n, π^*) terms into energetic level systems of molecules. The El-Sayed rule states [32] that intersystem crossing rate between excited states of different types exceeds that of the same type of excited states. Excited state energy level position depends on the solvent. For the similar ketocyanine dye, it was determined that the $^1(\pi, \pi^*)$ energy level lies above both $^3(n, \pi^*)$ and 3CT energy levels in nonpolar solvents (cyclohexane, toluene). In the case of polar solvents, $^1(\pi, \pi^*)$ lies above 3CT but below the $^3(n, \pi^*)$ energy level [25,31].

For closely related ketocyanine dye, the charge transfer state was established to be the lowest singlet state [31,33]. In nonpolar solvents such as toluene, the 1CT state lies above both $^3(n, \pi^*)$ and 3CT states, thus following the El-Sayed rule where ISC to $^3(n, \pi^*)$ first takes place and then IC quickly changes to the lowest 3CT state. However, due to relatively close proximity between the $^3(n, \pi^*)$ and 3CT state, the thermal population of $^3(n, \pi^*)$ occurs. This explains the high radical formation activity in toluene. In propanol-1, the 1CT state lies above 3CT but below $^3(n, \pi^*)$. Since ISC between 1CT and $^3(n, \pi^*)$ deals with the increase in energy, it is inefficient. Moreover, the transition between 1CT and 3CT is hindered, since the same type of excited states are involved. The energy gap between 3CT and $^3(n, \pi^*)$ is wider, so the thermal population role decreases. This explains both

lowered triplet state generation and decreased reactivity towards radical formation. Since the ordering of energy levels is the same in both acetonitrile and propanol-1, the probable explanation for high triplet generation efficiency in the case of the former solvent is the position of these levels: the $^3(n, \pi^*)$ state lies much closer to the 3CT state, which makes it easier for thermal population of $^3(n, \pi^*)$ to take place.

Due to the charge–transfer nature of the 4Met-BAC triplet state in propanol, it is easily stabilized by protic solvent molecules. In the case of acetonitrile, the triplet state is $^3(n, \pi^*)$ in nature and is less influenced by solvent molecules. The values of triplet state oxygen quenching rate constants (Table 3) were calculated according to following equation:

$$k = k_T + k_q[\text{O}_2] \quad (5)$$

where k_T is the triplet decay rate constant in the absence of oxygen (s^{-1}) (Equation (6)) and k_q is the triplet state oxygen quenching rate constant ($\text{M}^{-1}\text{s}^{-1}$) (Equation (7)).

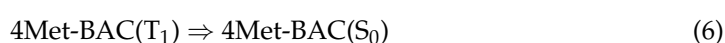


Table 3. 4Met-BAC triplet state characteristics in different conditions.

Solvent	k_T/s^{-1} Ar Purging	$k_{\text{O}_2}/\text{s}^{-1}$ O ₂ Purging	$k_{\text{diff}}/\text{M}^{-1}\text{s}^{-1}$	$1/9 k_{\text{diff}}/\text{M}^{-1}\text{s}^{-1}$	$k_q/\text{M}^{-1}\text{s}^{-1}$
Acetonitrile	8.0×10^6	4.5×10^7	1.9×10^{10}	2.1×10^9	3.1×10^9
Propanol	5.2×10^5	2.0×10^7	3.4×10^9	3.7×10^8	4.5×10^8

Calculation of the diffusional rate constant was performed using solvent viscosity according to [34]. The oxygen concentration values for different solvents were obtained according to [35,36]. The k_q values obtained for acetonitrile and propanol were close to k_{diff} multiplied by a spin-statistical factor of 1/9 (Table 3). These results are similar to the ones obtained in [31].

3.1.5. Singlet Oxygen Quantum Yield

The ability to generate singlet oxygen is related to intersystem crossing processes in photoinitiator molecules. Singlet oxygen forms as a result of energy transfer between the photoinitiator triplet state and molecular oxygen (Equation (7)):



The luminescence of singlet oxygen could be registered at ~ 1275 nm (Figure 7) (Equation (8)). The molecular surrounding of the solute fluorophore affects singlet oxygen generation efficiency (Table 2). In polar nonprotic solvent such as acetonitrile, 4Met-BAC exhibits a 20% increase in singlet oxygen production compared to MBAC. In propanol solution, this increase reaches almost 40%. This is due to hydrogen bonding 3CT triplet state stabilization.

The opposite situation is observed in the case of nonpolar solvents such as toluene. In the absence of the solvent stabilization effect, the role of vibrational relaxation increases for 4Met-BAC, and the role of intersystem crossing and fluorescence deactivation pathways diminishes.

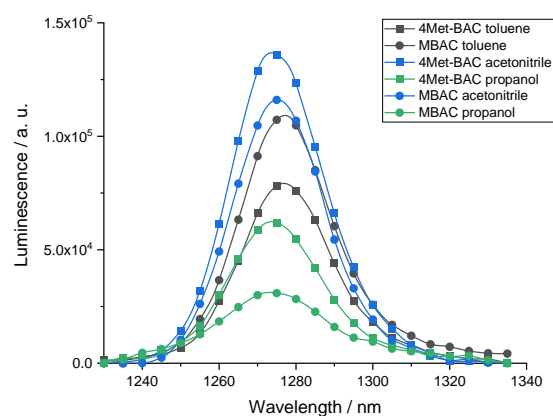
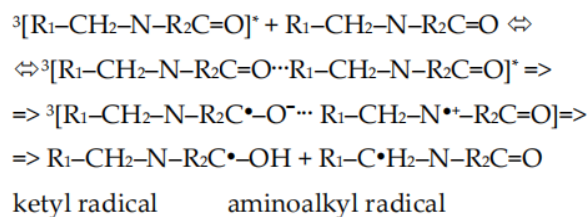


Figure 7. Singlet oxygen luminescence spectra of 4Met-BAC (6.0×10^{-6} M) (—■—) and MBAC (6.0×10^{-6} M) (—●—) solutions in different solvents. Excitation at 438–470 nm using a Xe lamp.

3.1.6. Radical Formation

It was previously proposed that radical initiation takes place as a result of electron transfer followed by proton transfer (ETPT), resulting in aminoalkyl and ketyl radical formation (Scheme 1) [37]. Unlike aminoalkyl radicals, ketyl radicals hardly initiate the polymerization process [38]. The formation of radical products probably occurs in the electron phototransfer process during interaction between the triplet state and the ground unexcited state of the photosensitizer.



Scheme 1. Proposed radical formation mechanism of 4Met-BAC.

In order to evaluate the input of radical formation for both 4Met-BAC and MBAC, a series of flash photolysis experiments were conducted using a conventional flash photolysis setup. Photobleaching of a singlet state in the region of 400–460 nm and radical absorption at a longer wavelength (480–540 nm) was registered (Figure 8).

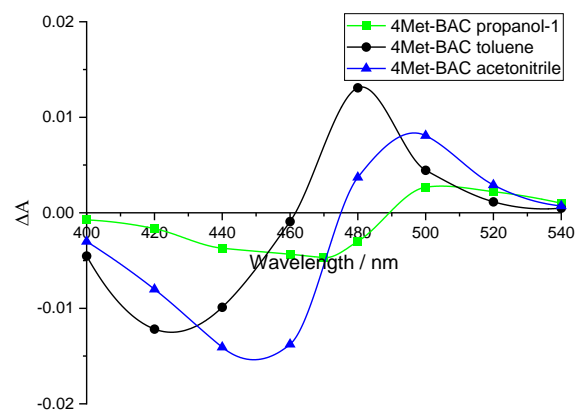


Figure 8. Differential transient absorption spectra of 4Met-BAC (7×10^{-7} M) in air-equilibrated solvents (green—propanol-1, black—toluene, blue—acetonitrile) 100 ms after flash.

The intensity of this absorption was different in various solvents. More intense radical formation was recorded in toluene and acetonitrile, where the triplet quantum yield was

most prominent. 4Met-BAC in propanol-1 showed the least power in terms of radical generation due to low triplet quantum yield and the different nature of the triplet state. Similar results were obtained for MBAC solutions (data not shown).

Deaerating the compound solution only resulted in increased signal intensity in the case of propanol-1 (Figure 9a), changing insignificantly in acetonitrile and toluene (data not shown).

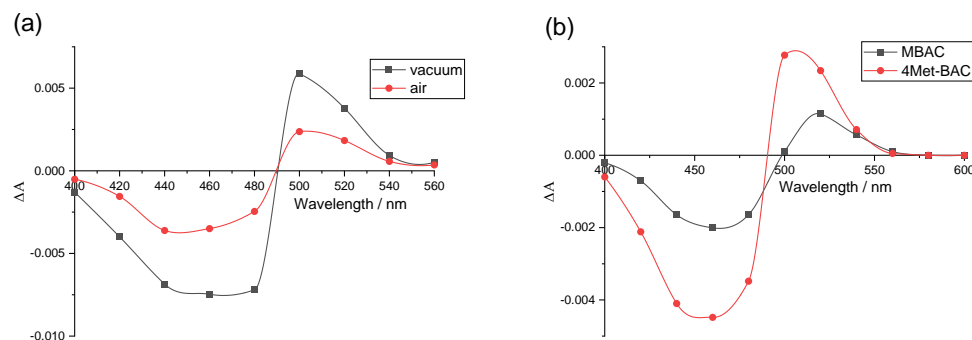


Figure 9. (a) Differential transient absorption spectra of 4Met-BAC (7×10^{-7} M) in propanol-1 100 ms after flash. (b) Differential transient absorption spectra of MBAC (1×10^{-6} M) and 4Met-BAC (1×10^{-6} M) in air-equilibrated propanol-1 50 ms after flash.

This observation corresponds to the oxygen quenching experiments. In the case of acetonitrile and toluene, the presence of oxygen weakly influenced the intensity of radical formation. Comparing MBAC and 4Met-BAC in terms of radical generation capability, one should note that, in propanol, 4Met-BAC radical absorption was significantly more intense MBAC radical absorption (Figure 9b), which corresponds with the singlet oxygen quantum yield results obtained earlier.

In this work, photopolymerization takes place in PETA monomer solution, thus providing polar and protic molecular surroundings for the photoinitiator. Taking PI alcohol solution as a model system, we established the enhanced intersystem crossing and radical generation ability of 4Met-BAC.

3.2. 3D Structure Fabrication

3.2.1. Influence of DLW Photolithography Parameters on Voxel Size in the TPP Process

The influence of DLW photolithography parameters on the physical properties of lithography elements (voxels) was investigated. To obtain the axial voxel size, the AFM method was used (Figure 10). For this study, samples consisting of linear voxel element arrays were fabricated. These were fabricated with different femtosecond laser radiation powers. Variation of the laser radiation power LP was carried out in the range of 3 to 10.5 mW. Within the array, the linear lithography speed V was varied from 120 to 180 $\mu\text{m/s}$, thus controlling exposure time. The obtained linear voxel elements on the substrate surface did not exceed 1.5 μm in height and had sufficient mechanical stability to preserve morphology during the development process.

The analytical dependence of volumetric lithography element half-height on the DLW photolithography parameters was obtained. This dependence was obtained by studying the two-photon polymerization model under the influence of femtosecond laser radiation. An approximation of the smallness of the radical diffusion rate was applied with respect to the polymerization rate of the exposed volume. The value (9) was used to analyze the results:

$$D_2 \propto \frac{NA^3 P^2}{\lambda^3 v} \propto \frac{P^2}{\delta_{Abbe}^3 v} \quad (9)$$

where $\delta_{Abbe} = \frac{1.22 \cdot \lambda}{2NA} = 340$ nm is the diffraction limit of Abbe. The quantity of D_2 is proportional to the Q-index used in [39], which allows for estimation of the influence of lens characteristics on polymerized volume size. The experimental dependence of the

half-height of the lithography volume element is approximated by the curve obtained by Equation (10):

$$h(D_2) = \frac{1}{2} * AR_2 * C * \delta_{Abbe} \sqrt{\left(\frac{D_2}{D_{th}}\right)^{\frac{2}{3}} - 1 - h_0} \quad (10)$$

where h is the measured height of the bulk element (nm), D_{th} is the threshold dose of radiation ($\text{mJ}^2/\mu\text{m}^4\text{s}$), h_0 is the height of focus deepening relative to the substrate border (nm), $C = 0.69$ is a constant value, and $AR_2 = 2$ is the ratio of the voxel's axial size to its lateral size. When $D_{th} = 0.024 \text{ mJ}^2/\mu\text{m}^4\text{s}$ and $h_0 = 450 \text{ nm}$, the mean square deviation of the experimental data from the theoretical approximation does not exceed 250 nm.

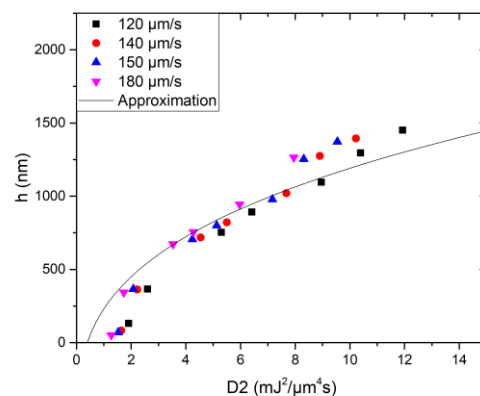


Figure 10. Dependence of volumetric lithography element half-height on the D_2 value.

3.2.2. Determination of the Degree of Conversion and Reduced Young's Modulus as Functions of Laser Power

The degree of conversion, DC, was investigated on polymer structures, which were parallelepipeds with a height of about $10 \mu\text{m}$ and a square cross-section of $25 \mu\text{m} \times 25 \mu\text{m}$. The distance between the layers was equal to the half-height of the lithography element (voxel) with the given lithography parameters obtained from previous studies. This was the case in order to control the pumped radiation dose, as well as to increase the height of the structures with fewer layers. All structures were fabricated at a constant hatching distance of $0.2 \mu\text{m}$. Linear lithography velocity was constant at $180 \mu\text{m}/\text{s}$. The structures were fabricated under different laser powers. The value of the conversion degree was calculated using Equation (11) [39,40].

$$DC = \left[1 - \frac{A_{C=C}^{poly} / A_{C=O}^{poly}}{A_{C=C}^{resin} / A_{C=O}^{resin}} \right] * 100\% \quad (11)$$

where are $A_{C=C}^{poly}$, $A_{C=O}^{poly}$, $A_{C=C}^{resin}$, and $A_{C=O}^{resin}$ represent signal integrals for C=C peaks and C=O peaks of polymerized and non-polymerized resin (Figure 11).

The obtained dependence (Figure 12) illustrates that conversion degree varies directly with laser power in the range of 0 to 5 mW. At laser power higher than 5 mW, conversion degree saturation reaches 34–36%.

Extrapolation of the degree of conversion (Figure 12) was performed using a simple model based on the threshold value [40] and the following Equation (12):

$$DC(LP) = [C_1 \left(1 - e^{-C_2 \left(\frac{LP}{LP_{th}} \right)^2} \right) + C_0] * 100\% \quad (12)$$

where $C_2 = 0.15$, $C_1 = 0.40$, and $C_0 = -0.05$ represent proportionality coefficients. $LP_{th} = 0.9 \text{ mW}$ was the threshold power for radiation used in this photocomposition. Coefficients C_1 and C_0 were chosen so that $C_1 + C_0 = DC_{saturation}$ and $DC(LP_{th}) = 0\%$. Additionally, coefficient

C_2 determines the exit to saturation speed of the conversion degree. Luminescence of the samples was also observed, which was caused by the fact that the photoinitiator is embedded in the polymer chain [24]. This feature of photocomposition can be applied in the study of structures using confocal microscopy [41].

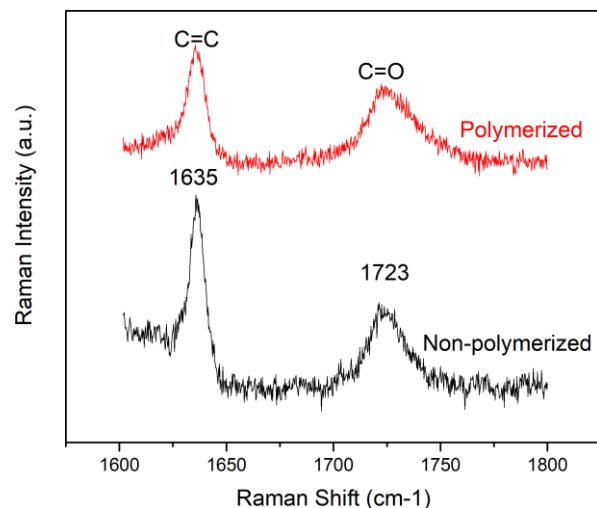


Figure 11. Raman spectrum of the polymerized and non-polymerized photocompositions (4Met-BAC and PETA). The spectra are shifted along the vertical axis for comparison. The black curve corresponds to the spectrum of the non-polymerized photocomposition. Red - for polymerized one.

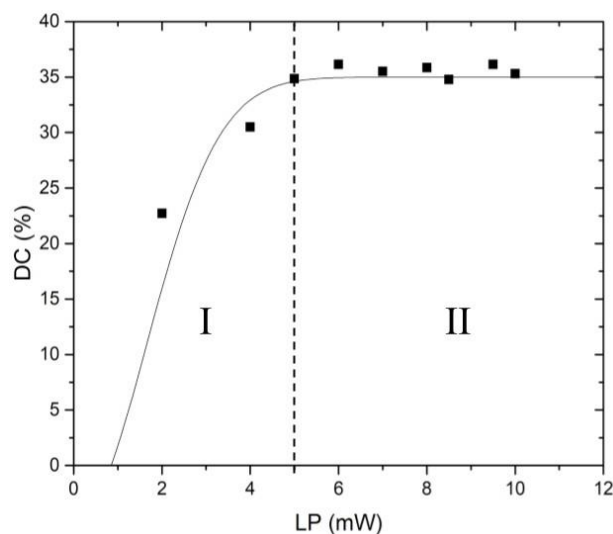


Figure 12. The dependence of conversion degree (DC) on laser power (LP). The solid line shows extrapolation starting from the threshold power of 0.9 mW. The dotted line separates regions I and II, where region I corresponds to conversion degree growth and region II corresponds to conversion degree.

3.2.3. Percolation Formation of Lines

In the process of studies of this photosensitive composition, an unaccounted mechanism for formation of polymerized regions was revealed. Thus, during sequential DLW photolithography of reference line elements (laser irradiation power exceeds the threshold power by an order of magnitude) with a small distance between the lines (order of magnitude of the diffraction limit), the space between them was filled with a thin polymer network, which was later well visualized by SEM. Polymer network formation is related to the diffusion of free monomer radicals and excited photoinitiator molecules in the volume of the photosensitive composition. Long-lived free radicals formed during exposure of the

photocomposition to femtosecond laser radiation remain near the polymerized volume in those regions of space, where their concentration is insufficient to form stable polymer chains. Random cross-linking of these radicals is the cause of polymer network formation. The formation mechanism of such polymer networks can be described using the percolation model [42–44]. The effect of polymer network formation by this physical mechanism can be applied to the lithography of tiny polymer nanostructures with sizes less than 100 nm [45].

The strategy for controlled formation of “percolation” polymer lines is based on the dynamics of free radical diffusion. Through ponderomotive forces and controlled generation of free radicals in near-threshold lithography, controlled formation of percolation lines/polymerization channels is possible. This strategy was applied to a photosensitive composition based on the 4Met-BAC photoinitiator and PETA monomer. Structures with special geometry were created for experiments on application of the percolation line formation control strategy (Figure 13a). The structures consisted of (1) a reference line array (lithography parameters: 20 mW, 170 $\mu\text{m/s}$) (horizontal lines on Figure 13a) and (2) a thin/percolation line array (vertical lines on Figure 13a) with a fixed distance between them (2 μm) and a lithography line speed of 170 $\mu\text{m/s}$. The distance between the reference lines varied from 1 to 4 μm . Thin lines were created with heights above the substrate of 0 to 0.5 μm and with power of 0.25 to 3 mW (threshold power value of 0.9 mW). Fabrication of structures with percolation lines was performed in the following sequence: DLW photolithography of the reference lines array (horizontal lines in Figure 13a,b) was first implemented, followed by thin percolation lines (vertical lines in Figure 13a,b). The sequence of line fabrication with DLW photolithography is important because the free radicals generated in the first step, during polymerization in close proximity to the reference lines, affect the thin-line lithography process in the second step.

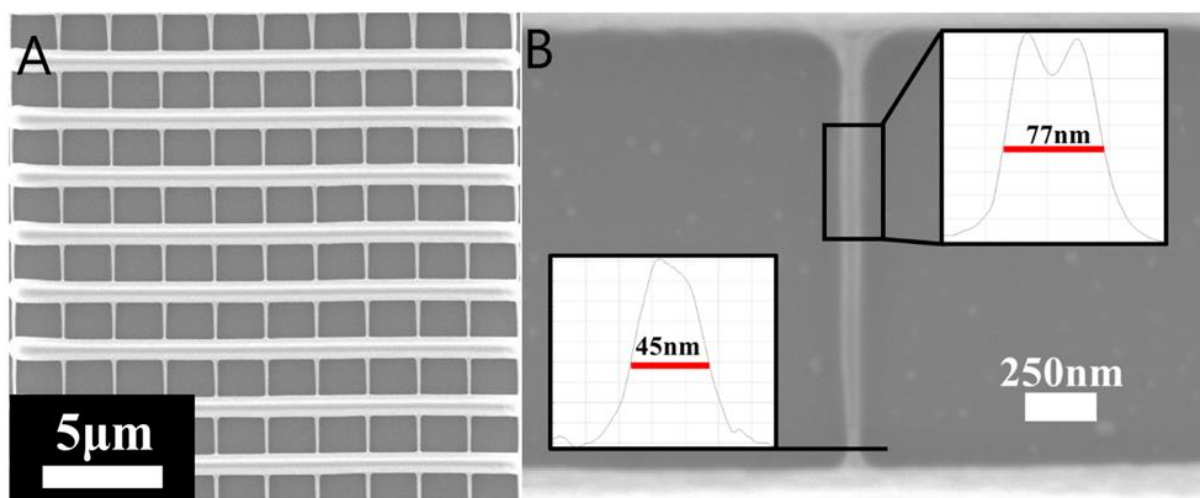


Figure 13. (A) SEM image of the structure with percolation lines (vertical). (B) SEM image of the percolation line with the smallest size. The insets show the electron scattering intensity profiles for the selected region.

As a result of this experiment, thin tiny polymer nanostructures with sizes less than 80 nm ($\lambda/10$ of the femtosecond wavelength) were obtained. One of the features of the obtained lines is the asymmetric shape. This type of shape is due to several factors. The lower broadening corresponds to a region with a higher concentration of free monomer radicals and a lower concentration of oxygen. As you move away from the reference lines, the concentration of free radicals decreases and the oxygen concentration reaches the average value in the composition, resulting in thinning of the line. At the same time, new radicals generated by laser radiation are captured in this region. The equilibrium state between the generated radicals and the laser radiation is reached only at a certain distance from the line. This causes a thinning near the beginning of the line (which is thinner than

the equilibrium line thickness). When approaching the reference lines, all equilibrium radicals are captured by free radicals near the line and, as a consequence, there is a strong thickening of the created line.

High repeatability of results is observed for the obtained lines. Among the created lines, line elements with sizes less than $\lambda/10$ were obtained, where λ is the wavelength of the laser radiation initiating the TPP process. Thus, the typical line obtained had a thickness at the equilibrium site of 77 nm, and at the narrowest site line thickness reached a value of 45 nm (Figure 13b). Linear element lithography with optimized parameters was performed with 1 mW photopolymerization laser power and a 2 μm gap.

The use of a physical percolation model in the fabrication of lightweight polymer structures makes it possible to create mechanically stable structures with a superresolution.

3.2.4. X-ray Lens Fabrication and Morphology

The achievement of surfaces in three-dimensional space with the required shape and high values of curvature is in demand for micro-optical element fabrication, including the fabrication of X-ray refractive microlenses. The use of such elements in 3D X-ray refractive microlenses is of interest in the X-ray microscopy field. This type of lens has a large number of advantages, such as quick alignment along the optical axis and the potential use of well-known methods of aberration improvement. The ability to achieve submicron feature size through DLW photolithography, as shown previously, could be used for smooth plastic micro-optics fabrication with nanometer precision. The DLW photolithography method allows one to fabricate 3D structures with arbitrary design. To demonstrate the effectiveness of such an approach, 3D X-ray refractive microlenses with aspherical shape were fabricated (Figure 14). A DLW photolithography algorithm was created in the DeScribe program. To obtain the smoothest surfaces, the structure parameters, the number of layers, the distance between linear elements, the radiation power for two-photon polymerization, and the linear lithography speed were optimized by utilizing the dependence of voxel size on DLW photolithography parameters (Figure 10). Among other things, a laser power above 5 mW was used so that the structure was mechanically stable (Figure 12, region II). Curvature radius of the X-ray lens was 10 μm , and the lens aperture was 24 μm .

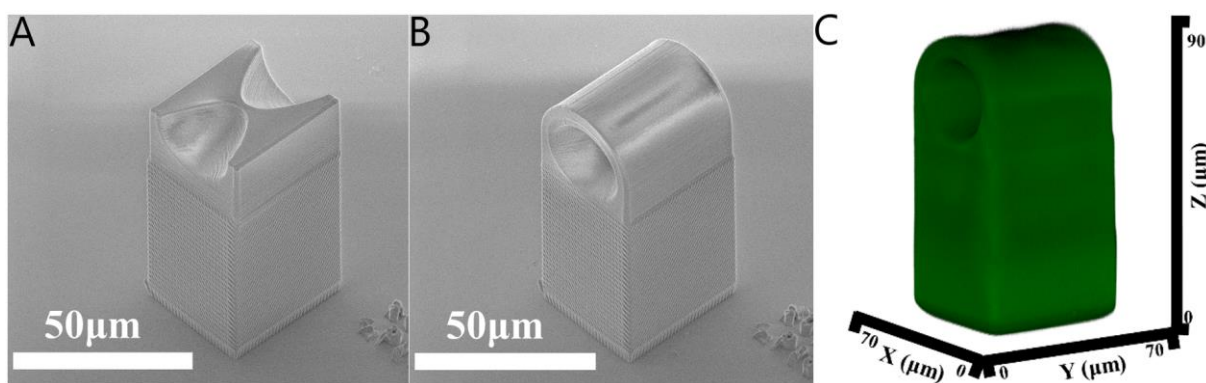


Figure 14. Aspherical lenses for X-rays. (A) SEM image of the cut structure. (B) SEM image of the structure. (C) CLSM image.

The morphology of this fabricated lens was investigated through Scanning Electron Microscopy (SEM) and Confocal Light Scanning Microscopy (CLSM). CLSM can be used for structures fabricated with DLW because of the strong luminescence of the tetramethacrylic benzylidene cyclopentanone dye integrated into the structure of polymer chains. CLSM and SEM could supplement each other. Analysis of X-ray lens morphology with SEM could provide one with full information about the roughness of surfaces. While using CLSM can provide information about the homogeneity of the physical properties of the X-ray lens polymer.

4. Discussion

The solvent effect plays a substantial role in deactivation pathways for MBAC and 4Met-BAC excited states. Protic conditions provide additional stabilization in 4Met-BAC molecules due to hydrogen bond formation with the four methyl methacrylate groups. As a result, fluorescence quantum yield and lifetime increase. Since PI triplet state is CT in nature in protic solvent, it is easily stabilized. Due to additional stabilization of triplet state 4Met-BAC in protic conditions, amplified singlet oxygen quantum yield is observed compared to MBAC. In toluene, the results are opposite: methyl methacrylate substituents provide additional options for vibrational relaxation processes, thus increasing the role of internal conversion and resulting in lower values of fluorescence and singlet oxygen quantum yield for 4Met-BAC. Since the polymerization conditions used in this work in terms of molecular surrounding are similar to PIs in alcohol solution, the latter could be considered as a model system for PI photochemical studies. Under these conditions, the methyl methacrylate derivative (4Met-BAC) shows increased triplet and radical generation ability, which alongside improved solubility in PETA monomer make it a more efficient photoinitiator.

Expanding concentration limits for this initiator in the composition allows for the photosensitivity of the composition to be controlled to a greater extent. Moreover, changes in the concentration of the photoinitiator in the composition do not significantly affect the physical and mechanical properties of the final polymer. These features are provided by chemical similarity between the photoinitiator and the monomer. Additionally, a high overexposure threshold can be associated with the inclusion of the photoinitiator molecules into the polymer chain. Experiments for investigation of the morphological and mechanical properties of polymerized areas during DLW photolithography were carried out with variations in laser power from 0 to 50 mW and varying lithography speeds of 1 to 200 $\mu\text{m}/\text{s}$. Based on this research, an anomalous behavior for laser lithography was determined. When linear lithography speed was in the range of 0 to 50 $\mu\text{m}/\text{s}$, a deviation from the monotonic voxel size increase with decreasing speed was observed. Additionally, lithographical mode increasing the conversion degree with an increase in laser power in the range of 0 to 5 mW was also discovered. A threshold dose value (radiation power of 5 mW at a speed of 180 $\mu\text{m}/\text{s}$) where the studied properties reach saturation values of $(35 \pm 1)\%$ were identified. These results make it possible to determine optimal parameters for lithography that allow for the production of mechanically stable structures.

5. Conclusions

Photochemical properties of a methacrylate benzylidene cyclopentanone derivative were studied. This PI possesses an enhanced ability to generate singlet oxygen and radical intermediates compared to the parent molecule in polar and protic surroundings similar to the PETA monomer environment. The experimental and analytical dependence of the size and elastic properties of voxels on the lithography parameters was established, which is important for the additive method of manufacturing 3D structures. These results make it possible to optimize algorithms for selecting lithography trajectory when creating continuous mechanically stable objects, such as micro-optical elements with high curvature values (including X-ray microlenses). The possibility of using a composition based on the 4Met-BAC photoinitiator to create microstructures for X-ray radiation is also justified due to the possibility of implementing sub-100 nm lithography with a smallest element size of 45 nm.

Supplementary Materials: The following supporting information can be downloaded at: <https://www.mdpi.com/article/10.3390/polym15010071/s1>, Figure S1: HNMR spectrum for 4Met-BAC; Figure S2: CNMR spectrum for 4Met-BAC.

Author Contributions: Conceptualization, A.G.V., V.A.K. and S.A.C.; methodology, A.A.K.; software, M.G.M.; validation, R.P.M.; formal analysis, R.P.M.; investigation, E.R.Z. and A.E.E.; resources, M.V.A.; data curation, I.D.B.; writing—original draft preparation, A.E.E. and D.A.S.; writing—review and editing, D.A.K., A.G.V. and V.A.K.; visualization, D.A.S.; supervision, D.A.C.; project administration, V.A.K.; funding acquisition, A.G.V. All authors have read and agreed to the published version of the manuscript.

Funding: This research was funded by the Russian Ministry of Science and Higher Education of the Russian Federation (project No.075-11-2021-086-MIPT) and partly by RSF Project №22-19-00324 (Creation of optical fibers on a chip with characteristic dimensions less than 100 nm).

Institutional Review Board Statement: Not applicable.

Informed Consent Statement: Not applicable.

Data Availability Statement: Not applicable.

Acknowledgments: The authors acknowledge the MIPT Shared Facilities Center and Evgeny Korostylev personally for their help in studying the morphology of the “percolation” structures through scanning electron microscopy. The authors are grateful for useful discussions and SEM investigation provided by the staff of Moscow State University: M. Sharipova, T. Baluyan, and A. Fedyanin. Spectral measurements were performed at the Shared Research Facilities of IBCP RAS “New Materials and Technologies” according to the state task “Kinetics and mechanism of elementary stages of complex photochemical processes”.

Conflicts of Interest: The authors declare no conflict of interest.

References

1. Bagheri, A.; Jin, J. Photopolymerization in 3D Printing. *ACS Appl. Polym. Mater.* **2019**, *1*, 593–611. [[CrossRef](#)]
2. Faraji, Z.R.; Prewett, P.D.; Davies, G.J. High-resolution two-photon polymerization: The most versatile technique for the fabrication of microneedle arrays. *Microsyst Nanoeng.* **2021**, *7*, 71. [[CrossRef](#)] [[PubMed](#)]
3. Aeby, S.; Aubry, G.J.; Muller, N.; Scheffold, F. Scattering from Controlled Defects in Woodpile Photonic Crystals. *Adv. Opt. Mater.* **2021**, *9*, 2001699. [[CrossRef](#)]
4. Liu, Y.; Wang, H.; Ho, J.; Ng, R.C.; Ng, R.J.H.; Hall-Chen, V.H.; Koay, E.H.H.; Dong, Z.; Liu, H.; Qiu, C.W.; et al. Structural Color Three-Dimensional Printing by Shrinking Photonic Crystals. *Nat. Commun.* **2019**, *10*, 4340. [[CrossRef](#)]
5. Ji, Q.; Moughames, J.; Chen, X.; Fang, G.; Huaroto, J.J.; Laude, V.; Martínez, J.A.I.; Ulliac, G.; Clévy, C.; Lutz, P.; et al. 4D Thermomechanical Metamaterials for Soft Microrobotics. *Commun. Mater.* **2021**, *2*, 93. [[CrossRef](#)]
6. Lio, G.E.; Ferraro, A.; Ritacco, T.; Aceti, D.M.; De Luca, A.; Giocondo, M.; Caputo, R. Leveraging on ENZ Metamaterials to Achieve 2D and 3D Hyper-Resolution in Two-Photon Direct Laser Writing. *Adv. Mat.* **2021**, *33*, 2008644. [[CrossRef](#)]
7. Bückmann, T.; Schittny, R.; Thiel, M.; Kadic, M.; Milton, G.W.; Wegener, M. On Three-Dimensional Dilational Elastic Metamaterials. *New J. Phys.* **2014**, *16*, 033032. [[CrossRef](#)]
8. Maciulaitis, J.; Rekštytė, S.; Bratchikov, M.; Gudas, R.; Malinauskas, M.; Pockevicius, A.; Usas, A.; Rimkunas, A.; Jankauskaite, V.; Grigaliunas, V.; et al. Customization of direct laser lithography-based 3D scaffolds for optimized in vivo outcome. *Appl. Surf. Sci.* **2019**, *487*, 692–702. [[CrossRef](#)]
9. Vanderpoorten, O.; Peter, Q.; Challa, P.K.; Keyser, U.F.; Baumberg, J.; Kaminski, C.F.; Knowles, T.P.J. Scalable integration of nano- and microfluidics with hybrid two-photon lithography. *Microsyst Nanoeng.* **2019**, *5*, 40. [[CrossRef](#)]
10. Amato, L.; Gu, Y.; Bellini, N.; Eaton, S.M.; Cerullo, G.; Osellame, R. Integrated Three-Dimensional Filter Separates Nanoscale from Microscale Elements in a Microfluidic Chip. *Lab Chip.* **2012**, *12*, 1135–1142. [[CrossRef](#)]
11. Li, J.; Fejes, L.; Lorensen, D.; Quirk, B.C.; Noble, P.B.; Kirk, R.W.; Orth, A.; Wood, F.M.; Gibson, B.C.; Sampson, D.D.; et al. Two-photon polymerisation 3D printed freeform micro-optics for optical coherence tomography fibre probes. *Sci. Rep.* **2018**, *8*, 14789. [[CrossRef](#)] [[PubMed](#)]
12. Gonzalez-Hernandez, D.; Varapnickas, S.; Merkininkaitė, G.; Čiburys, A.; Gailevičius, D.; Šakirzanovas, S.; Juodkakis, S.; Malinauskas, M. Laser 3D Printing of Inorganic Free-Form Micro-Optics. *Photonics* **2021**, *8*, 577. [[CrossRef](#)]
13. Schell, A.W.; Neumer, T.; Shi, Q.; Kaschke, J.; Fischer, J.; Wegener, M.; Benson, O. Laser-Written Parabolic Micro-Antennas for Efficient Photon Collection. *Appl. Phys. Lett.* **2014**, *105*, 231117. [[CrossRef](#)]
14. Wang, H.; Wang, H.; Zhang, W.; Yang, J.K.W. Toward Near-Perfect Diffractive Optical Elements via Nanoscale 3D Printing. *ACS Nano.* **2020**, *14*, 10452–10461. [[CrossRef](#)]
15. Asadollahbaik, A.; Thiele, S.; Weber, K.; Kumar, A.; Drozella, J.; Sterl, F.; Herkommer, A.M.; Giessen, H.; Fick, J. Highly Efficient Dual-Fiber Optical Trapping with 3D Printed Diffractive Fresnel Lenses. *ACS Photonics* **2020**, *7*, 88–97. [[CrossRef](#)]

16. Pawar, A.A.; Halivni, S.; Waiskopf, N.; Ben-Shahar, Y.; Soreni-Harari, M.; Bergbreiter, S.; Banin, U.; Magdassi, S. Rapid Three-Dimensional Printing in Water Using Semiconductor-Metal Hybrid Nanoparticles as Photoinitiators. *Nano Lett.* **2017**, *17*, 4497–4501. [[CrossRef](#)]
17. Zhu, Y.; Liu, Y.; Miller, K.A.; Zhu, H.; Egap, E. Lead Halide Perovskite Nanocrystals as Photocatalysts for PET-RAFT Polymerization under Visible and Near-Infrared Irradiation. *ACS Macro Lett.* **2020**, *9*, 725–730. [[CrossRef](#)] [[PubMed](#)]
18. Lyubomirskiy, M.; Koch, F.; Abrashitova, K.A.; Bessonov, V.O.; Kokareva, N.; Petrov, A.; Seiboth, F.; Wittwer, F.; Kahnt, M.; Seyrich, M.; et al. Ptychographic Characterisation of Polymer Compound Refractive Lenses Manufactured by Additive Technology. *Opt. Express* **2019**, *27*, 8639–8650. [[CrossRef](#)]
19. Sharipova, M.I.; Baluyan, T.G.; Abrashitova, K.A.; Kulagin, G.E.; Petrov, A.K.; Chizhov, A.S.; Shatalova, T.B.; Chubich, D.; Kolymagin, D.A.; Vitukhnovsky, A.G.; et al. Effect of Pyrolysis on Microstructures Made of Various Photoresists by Two-Photon Polymerization: Comparative Study. *Opt. Mater. Express* **2021**, *11*, 371–384. [[CrossRef](#)]
20. Dumur, F. Recent Advances on Benzylidene Ketones as Photoinitiators of Polymerization. *Eur. Polym. J.* **2022**, *178*, 111500. [[CrossRef](#)]
21. Fu, H.; Qiu, Y.; You, J.; Hao, T.; Fan, B.; Nie, J.; Wang, T. Photopolymerization of Acrylate Resin and Ceramic Suspensions with Benzylidene Ketones under Blue/Green LED. *Polymer* **2019**, *184*, 121841. [[CrossRef](#)]
22. Armarego, W.L.F. Purification of Laboratory Chemicals. In *Butterworth-Heinemann*, 8th ed.; Butterworth-Heinemann: Oxford, UK, 2017.
23. Vatsadze, S.Z.; Gavrilova, G.V.; Zyuz'kevich, F.S.; Nuriev, V.N.; Krut'ko, D.P.; Moiseeva, A.A.; Shumyantsev, A.V.; Vedernikov, A.I.; Churakov, A.V.; Kuz'mina, L.G.; et al. Synthesis, structure, electrochemistry, and photophysics of 2,5-dibenzylidenecyclopentanones containing in benzene rings substituents different in polarity. *Russ. Chem. Bull.* **2016**, *65*, 1761–1772. [[CrossRef](#)]
24. Zhiganshina, E.R.; Arsenyev, M.V.; Chubich, D.A.; Kolymagin, D.A.; Pisarenko, A.V.; Burkatovsky, D.S.; Baranov, E.V.; Vitukhnovsky, A.G.; Lobanov, A.N.; Matital, R.P.; et al. Tetramethacrylic Benzylidene Cyclopentanone Dye for One- and Two-Photon Photopolymerization. *Eur. Polym. J.* **2022**, *162*, 110917. [[CrossRef](#)]
25. Li, Z.; Pucher, N.; Cicha, K.; Torgersen, J.; Ligon, S.C.; Ajami, A.; Husinsky, W.; Rosspointner, A.; Vauthey, E.; Naumov, S.; et al. A Straightforward Synthesis and Structure-Activity Relationship of Highly Efficient Initiators for Two-Photon Polymerization. *Macromolecules* **2013**, *46*, 352–361. [[CrossRef](#)]
26. Pivovarenko, V.G.; Klueva, A.V.; Doroshenko, A.O.; Demchenko, A.P. Bands separation in fluorescence spectra of ketocyanine dyes: Evidence for their complex formation with monohydric alcohols. *Chem. Phys. Lett.* **2000**, *325*, 389–398. [[CrossRef](#)]
27. Parkanyi, C.; Rao Oruganti, S.; Szentpaly, V.; Ngom, B.; Aaron, J. Dipole moments of indoles in their ground and the first excited singlet states. *J. Mol. Str. Theochem.* **1986**, *135*, 105–116. [[CrossRef](#)]
28. Belay, A.; Libnedengel, E.; Kim, H.K.; Hwang, Y.H. Effects of Solvent Polarity on the Absorption and Fluorescence Spectra of Chlorogenic Acid and Caffeic Acid Compounds: Determination of the Dipole Moments. *Luminescence* **2016**, *31*, 118–126. [[CrossRef](#)]
29. Aaron, J.J.; Buna, M.; Parkanyi, C.; Shafik Antonious, M.; Tine, A.; Cisse, L. Quantitative Treatment of the Effect of Solvent on the Electronic Absorption and Fluorescence Spectra of Substituted Coumarins: Evaluation of the First Excited Singlet-State Dipole Moments. *J. Fluoresc.* **1995**, *5*, 337–347. [[CrossRef](#)]
30. Marcotte, N.; Fery-Forgues, S. Influence of a Second Donor and of Rotational Isomers on the Solvatochromic Properties of Ketocyanine Fluorophores. *J. Chem. Soc. Perkin Trans.* **2000**, *2*, 1711–1716. [[CrossRef](#)]
31. Bamabas, M.V.; Liu, A.; Trifunac, A.D.; Krongauz, V.V.; Chang, C.T. Solvent Effects on the Photochemistry of a Ketocyanine Dye and Its Functional Analogue, Michler's Ketone. *J. Phys. Chem.* **1992**, *96*, 212–217.
32. El-Sayed, M.A. Spin-Orbit Coupling and the Radiationless Processes in Nitrogen Heterocycles. *J. Chem. Phys.* **1963**, *38*, 2834–2838. [[CrossRef](#)]
33. Brown, R.G.; Porter, G. Photochemistry of Michler's Ketone in Cyclohexane and Alcohol Solvents. *J. Chem. Soc. Faraday Trans.* **1977**, *1*, 1569–1573. [[CrossRef](#)]
34. Reynolds, E.W.; Demas, J.N.; Degraff, B.A. Viscosity and Temperature Effects on the Rate of Oxygen Quenching of Tris-(2,2'-Bipyridine)Ruthenium(II). *J. Fluoresc.* **2013**, *23*, 237–241. [[CrossRef](#)] [[PubMed](#)]
35. Sato, T.; Hamada, Y.; Sumikawa, M.; Araki, S.; Yamamoto, H. Solubility of Oxygen in Organic Solvents and Calculation of the Hansen Solubility Parameters of Oxygen. *Ind. Eng. Chem. Res.* **2014**, *53*, 19331–19337. [[CrossRef](#)]
36. Franco, C.; Iii, J.O. Photochemical determination of the solubility of oxygen in various media. *Talanta* **1990**, *37*, 905–909. [[CrossRef](#)]
37. Huang, X.; Zhang, Y.; Shi, M.; Zhang, Y.; Zhao, Y. Study on a Polymerizable Visible Light Initiator for Fabrication of Biosafety Materials. *Polym. Chem.* **2019**, *10*, 2273–2281. [[CrossRef](#)]
38. Christmann, J.; Allonas, X.; Ley, C.; Croutxé-Barghorn, C. The Role of Ketyl Radicals in Free Radical Photopolymerization: New Experimental and Theoretical Insights. *Polym. Chem.* **2019**, *10*, 1099–1109. [[CrossRef](#)]
39. Jiang, L.J.; Zhou, Y.S.; Xiong, W.; Gao, Y.; Huang, X.; Jiang, L.; Baldacchini, T.; Silvain, J.-F.; Lu, Y.F. Two-Photon Polymerization: Investigation of Chemical and Mechanical Properties of Resins Using Raman Microspectroscopy. *Opt. Lett.* **2014**, *39*, 3034–3037. [[CrossRef](#)]
40. Bauer, J.; Guell Izard, A.; Zhang, Y.; Baldacchini, T.; Valdevit, L. Programmable Mechanical Properties of Two-Photon Polymerized Materials: From Nanowires to Bulk. *Adv. Mater. Technol.* **2019**, *4*, 1900146. [[CrossRef](#)]

41. Matital, R.P.; Kolymagin, D.A.; Chubich, D.A.; Merkushev, D.D.; Vitukhnovsky, A.G. Luminescence Confocal Microscopy of 3D Components of Photonic Integrated Circuits Fabricated by Two-Photon Photopolymerization. *J. Sci. Adv. Mat. Dev.* **2022**, *7*, 100413. [[CrossRef](#)]
42. Flory, P.J. Molecular Size Distribution in Three Dimensional Polymers. I. Gelation. *J. Am. Chem. Soc.* **1941**, *63*, 3083–3090. [[CrossRef](#)]
43. Flory, P.J. Molecular Size Distribution in Three Dimensional Polymers. II. Trifunctional Branching Units. *J. Am. Chem. Soc.* **1941**, *63*, 3091–3096. [[CrossRef](#)]
44. Stockmayer, W.H. Theory of Molecular Size Distribution and Gel Formation in Branched-Chain Polymers. *J. Chem. Phys.* **1943**, *11*, 45–55. [[CrossRef](#)]
45. Wang, S.; Yu, Y.; Liu, H.; Lim, K.T.P.; Srinivasan, B.M.; Zhang, Y.W.; Yang, J.K.W. Sub-10-Nm Suspended Nano-Web Formation by Direct Laser Writing. *Nano Futures* **2018**, *2*, 025006. [[CrossRef](#)]

Disclaimer/Publisher’s Note: The statements, opinions and data contained in all publications are solely those of the individual author(s) and contributor(s) and not of MDPI and/or the editor(s). MDPI and/or the editor(s) disclaim responsibility for any injury to people or property resulting from any ideas, methods, instructions or products referred to in the content.